Journal of Materials Chemistry C

ROYAL SOCIETY OF CHEMISTRY

PAPER

View Article Online
View Journal | View Issue

Cite this: J. Mater. Chem. C, 2025, 13, 19383

Bandgap engineering in quasi-1D $Zr_{1-x}Ti_xS_3$ ($0 \leq x \leq 1$) solid solutions

Dmitry S. Muratov, *[a] Ettore Bianco, [a] Dmitry Karpenkov, [b] Alberto Castellero, [a] Alexey Lipatov, [c] Valter Maurino [a] and Alexander Sinitskii *[de]

TiS_3 and ZrS_3 are quasi-one-dimensional materials from the family of transition metal trichalcogenides with the general composition MX_3, where M is a transition metal and X is a chalcogen. Although isostructural, TiS_3 and ZrS_3 have very different bandgaps of approximately 1 eV and 2 eV, respectively. Consequently, $Zr_{1-x}Ti_xS_3$ solid solutions are promising for achieving a composition-dependent bandgap that is tunable across a broad spectral range, from visible to infrared, for various electronic and optoelectronic applications. Previous studies demonstrated the synthesis of $Zr_{1-x}Ti_xS_3$ solid solutions from elemental precursors at 800 °C, but only in a narrow compositional range of $0 \leq x \leq 0.33$, while higher Ti content led to the formation of a secondary TiS_2 phase. In this work, we optimized the synthetic conditions and produced the entire range of $Zr_{1-x}Ti_xS_3$ solid solutions ($0 \leq x \leq 1$) *via* a direct reaction between Zr–Ti alloys and sulfur vapor at a lower temperature of 600 °C. All $Zr_{1-x}Ti_xS_3$ compositions crystallized as needle-like structures within the $P2_1/m$ space group, with lattice parameters increasing with the Zr content, as confirmed by X-ray diffraction analysis. The optical bandgaps of the prepared crystals were within the 1 to 2 eV range and also increased with the Zr content, demonstrating that synthesis of $Zr_{1-x}Ti_xS_3$ solid solutions is a viable route for bandgap engineering in transition metal trichalcogenides.

Received 28th June 2025,
Accepted 7th August 2025

DOI: 10.1039/d5tc02480c

rsc.li/materials-c

Introduction

Transition metal trichalcogenides (TMTCs) are quasi-one-dimensional (quasi-1D) materials with the general composition MX_3, where M is a transition metal such as Ti, Zr, Hf, Ta, or Nb and X is S, Se, or Te.[1–5] Members of the TMTC family exhibit intriguing physical phenomena, including temperature-dependent metal–insulator transitions, charge density waves, and superconductivity,[3–8] possess remarkable properties, such as anisotropic electronic transport[9–12] and high breakdown current densities,[13,14] and show promise for numerous electronic and optoelectronic applications,[5,15] ranging from field-effect transistors,[11,16,17] polarization-sensitive photodetectors,[18–21] and printed electronics[22] to thermoelectric converters,[23,24] gas sensors,[25–28] and charge transport materials in light-emitting devices.[29] Many of these applications benefit from the variable bandgaps of TMTCs that can be either metallic, such as TaS_3 and $NbSe_3$, have small bandgaps of about 1 eV or less, such as TiS_3, $ZrSe_3$, and $HfSe_3$, or have bandgaps around 2 eV or larger, such as ZrS_3 and HfS_3.[5] Interestingly, despite the great diversity of TMTC materials, they do not cover the visible-to-near-infrared range from 1 to 2 eV, which is crucial for many optoelectronic and photonic technologies. Materials with bandgaps in this range are commonly used for efficient light absorption and charge carrier generation in photovoltaic devices.[30] They are also employed in light-emitting devices and photodetectors for telecommunications, integrated photonics, biomedical imaging, and many other applications. Therefore, the potential applications of TMTCs could be significantly expanded if these materials were engineered to exhibit tunable bandgaps within the 1–2 eV range.

In this work, for the bandgap engineering in TMTCs we considered solid solutions of TiS_3 and ZrS_3. These are isostructural compounds that have a monoclinic $ZrSe_3$-type crystal structure (space group $P2_1/m$) that is schematically shown in Fig. 1a and b. TiS_3 has a bandgap of about 1 eV,[31–33] while ZrS_3 has a larger bandgap of about 2 eV.[2,12,34,35] Therefore, $Zr_{1-x}Ti_xS_3$ solid solutions ($0 \leq x \leq 1$) provide a promising material platform for realizing a composition-dependent

[a] Department of Chemistry, University of Turin, Turin, 10125, Italy. E-mail: dmitry.muratov@unito.it
[b] Department of Magnetism, Lomonosov Moscow State University, Leninskie Gory, Moscow, 119991, Russia
[c] Department of Chemistry, Biology & Health Sciences, South Dakota Mines and Technology, Rapid City, SD57701, USA
[d] Department of Chemistry, University of Nebraska-Lincoln, Lincoln, NE 68588, USA. E-mail: sinitskii@unl.edu
[e] Nebraska Center of Materials and Nanoscience, University of Nebraska-Lincoln, Lincoln, NE 68588, USA

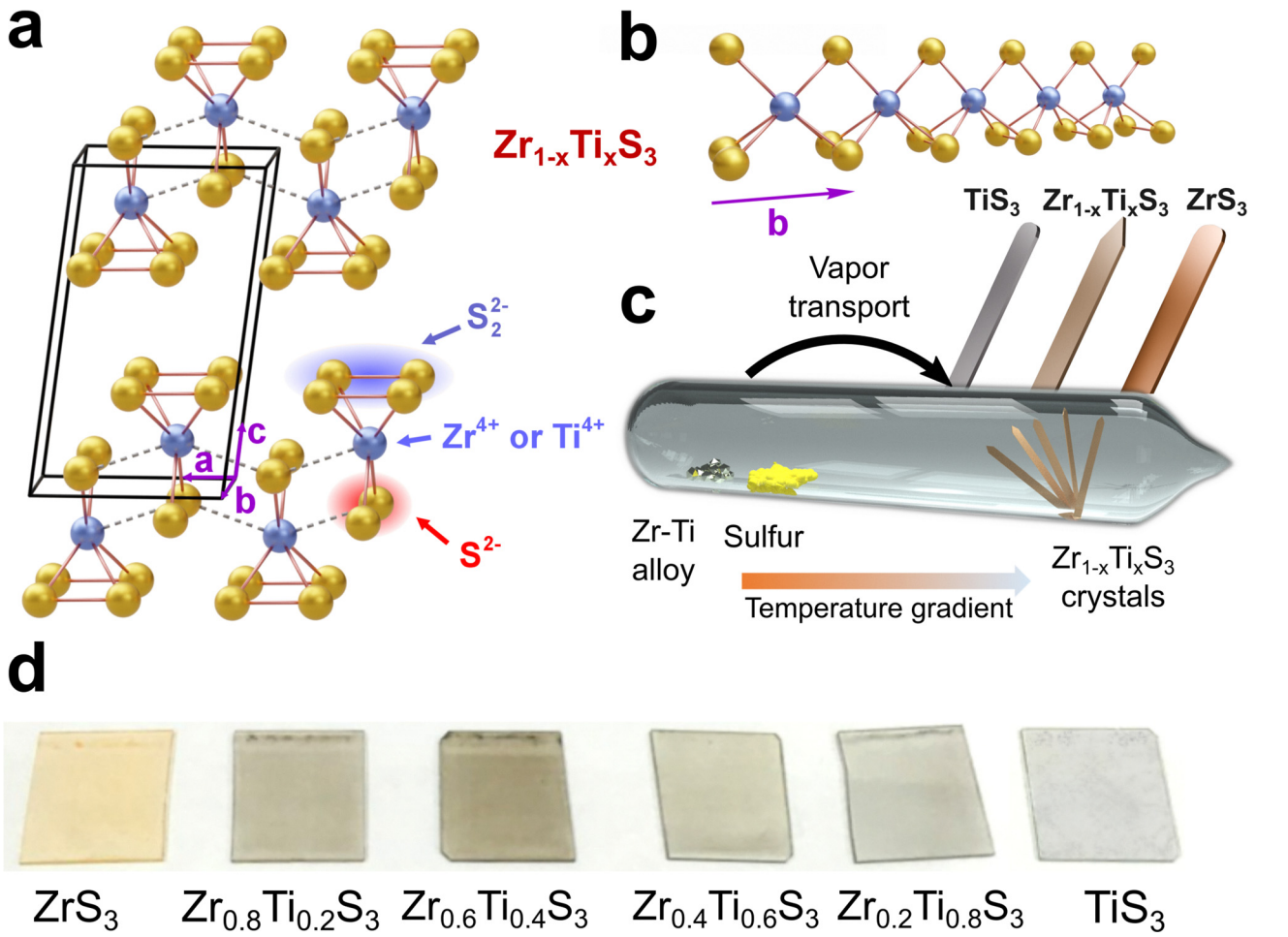

Fig. 1 (a) Scheme of crystal structure and unit cell of $Zr_{1-x}Ti_xS_3$ solid solution. (b) Scheme of 1D chain of $Zr_{1-x}Ti_xS_3$ solid solution along the *b* crystallographic direction. (c) Scheme of the chemical vapor transport method used to obtain $Zr_{1-x}Ti_xS_3$ with crystal shape illustrations for TiS_3, ZrS_3 and $Zr_{1-x}Ti_xS_3$ solid solutions. (d) Photographs of glass slides with slot-die printed layers of the full range of $Zr_{1-x}Ti_xS_3$ solid solutions.

bandgap that is tunable across a broad spectral range, from visible to infrared.

Several previous works focused on the synthesis and characterization of $Zr_{1-x}Ti_xS_3$ solid solutions.[36–39] Gard and co-workers performed spectroscopic studies of $Zr_{1-x}Ti_xS_3$ ($0 \leq x \leq 1$) crystals[37] although did not disclose their preparation and referenced a prior study.[36] However, that study by Sieber and co-workers, which investigated chemical vapor transport reaction between metallic Ti, Zr and sulfur vapor at 800 °C, reported the synthesis of $Zr_{1-x}Ti_xS_3$ solid solutions only with $0 \leq x \leq 0.33$.[36] We also studied the reaction between the metals and sulfur at 800 °C and reached a similar conclusion that under these conditions the $Zr_{1-x}Ti_xS_3$ solid solutions can only be obtained in a narrow compositional range.[39] When a high titanium content is used in the precursor mixture, the resulting $Zr_{1-x}Ti_xS_3$ crystals still have $x < 0.33$, while the Ti excess results in the formation of a secondary TiS_2 phase.[39] Therefore, while prior literature suggests that $Zr_{1-x}Ti_xS_3$ solid solutions with $x > 0.33$ are realistic, the procedure for their synthesis remains missing in literature. In this study, we aimed to address this gap in knowledge and establish synthetic procedures for the entire series of solid solutions with $0 \leq x \leq 1$, which is necessary to cover the whole 1–2 eV range of bandgaps with $Zr_{1-x}Ti_xS_3$ compounds.

We optimized the synthetic conditions and produced the entire range of $Zr_{1-x}Ti_xS_3$ solid solutions ($0 \leq x \leq 1$) *via* a direct reaction between Zr–Ti alloys and sulfur vapor at a lower temperature of 600 °C. We demonstrate that the resulting $Zr_{1-x}Ti_xS_3$ compositions formed needle-like crystals, consistent with the quasi-1D structure of $ZrSe_3$-type compounds. The lattice parameters of $Zr_{1-x}Ti_xS_3$ solid solutions systematically increased with the Zr content, as confirmed by X-ray diffraction analysis. The optical bandgaps of the prepared crystals were within the 1 to 2 eV range and linearly increased with the Zr content, demonstrating that $Zr_{1-x}Ti_xS_3$ solid solutions are viable route for bandgap engineering in TMTC materials for electronic and optoelectronic applications.

Results and discussion

Previous reports on the synthesis of $Zr_{1-x}Ti_xS_3$ crystals utilized pure powders of Ti and Zr as precursors and noted that even

when employing high titanium-to-zirconium ratios, the resulting solid solutions were deficient in titanium.[36,38,39] This could be due to the difference in the vapor pressures of Ti and Zr under the chosen synthetic conditions. Our approach, involving precisely controlled $Zr_{1-x}Ti_x$ alloys instead of mixtures of elemental Zr and Ti (Fig. 1c), aimed to achieve a more even evaporation of the metallic precursors.[39] However, we also observed a reduced titanium concentration in the produced $Zr_{1-x}Ti_xS_3$ solid solutions when the ampoules were annealed at 800 °C.[39] In this study, we attempted synthesis of $Zr_{1-x}Ti_xS_3$ crystals at different temperatures and found that when the temperature is reduced from 800 °C to 600 °C, the resulting solid solutions have the same Ti/Zr ratio as in the precursor alloys. The reaction products were imaged by optical (Fig. 1d) and scanning electron microscopy (SEM), and their composition was confirmed by energy-dispersive X-ray spectroscopy (EDX), see Fig. S1–S4. In Fig. 2, we demonstrate SEM images of all $Zr_{1-x}Ti_xS_3$ crystals as well as provide EDX mapping data for $Zr_{0.2}Ti_{0.8}S_3$, the solid solution with the highest titanium content, while EDX maps for other compositions are shown in Fig. S5. The maps show that for all $Zr_{1-x}Ti_xS_3$ compositions the elements are evenly distributed throughout the crystals.

Most of the $Zr_{1-x}Ti_xS_3$ crystals had similar shapes across different Ti/Zr ratios. The ends of the solid solution crystals were typically sharp, resembling a sword tip, while pure ZrS_3 and TiS_3 crystals had rounded tips, see Fig. 2 as well as Fig. S6 and S7. Based on the shapes of these needle-like crystals, it can be concluded that the fastest growth occurs in the *b* direction of 1D chains in the structure (Fig. 1b). According to the Burton–Cabrera–Frank (BCF) theory of crystal growth mechanics,[40] the surface of a growing crystal needs an atomic kink or an open step to promote further growth. For a $Zr_{1-x}Ti_xS_3$ solid solution crystal, particularly when the Ti/Zr ratio is about 1 : 1, this kink forms naturally due to the presence of two types of atoms with the same number of valence electrons but differing atomic radii (0.160 nm for Zr and 0.147 nm for Ti). This difference in atomic radii significantly accelerates growth along the *b* direction, giving the crystals their sword-like shapes. The 'sword' edges could be formed by the planes with high-*h* (*h*11) Miller indices, where $h > 3$. These planes form because of the large discrepancy between the growth rates along the *b* direction and at oblique angles to it. A simple evaluation of the crystal shapes indicates that the growth rate along the *b* direction should be at least three times higher for the $Zr_{1-x}Ti_xS_3$ solid solutions compared to pristine ZrS_3 and TiS_3 under the same conditions (Fig. S8).

We found that the size of the crystals strongly depends on the Ti/Zr ratio in the resulting solid solution. At high Ti/Zr ratios, the crystals grow significantly larger, reaching widths greater than 5 or even 10 μm. In contrast, at lower Ti/Zr ratios,

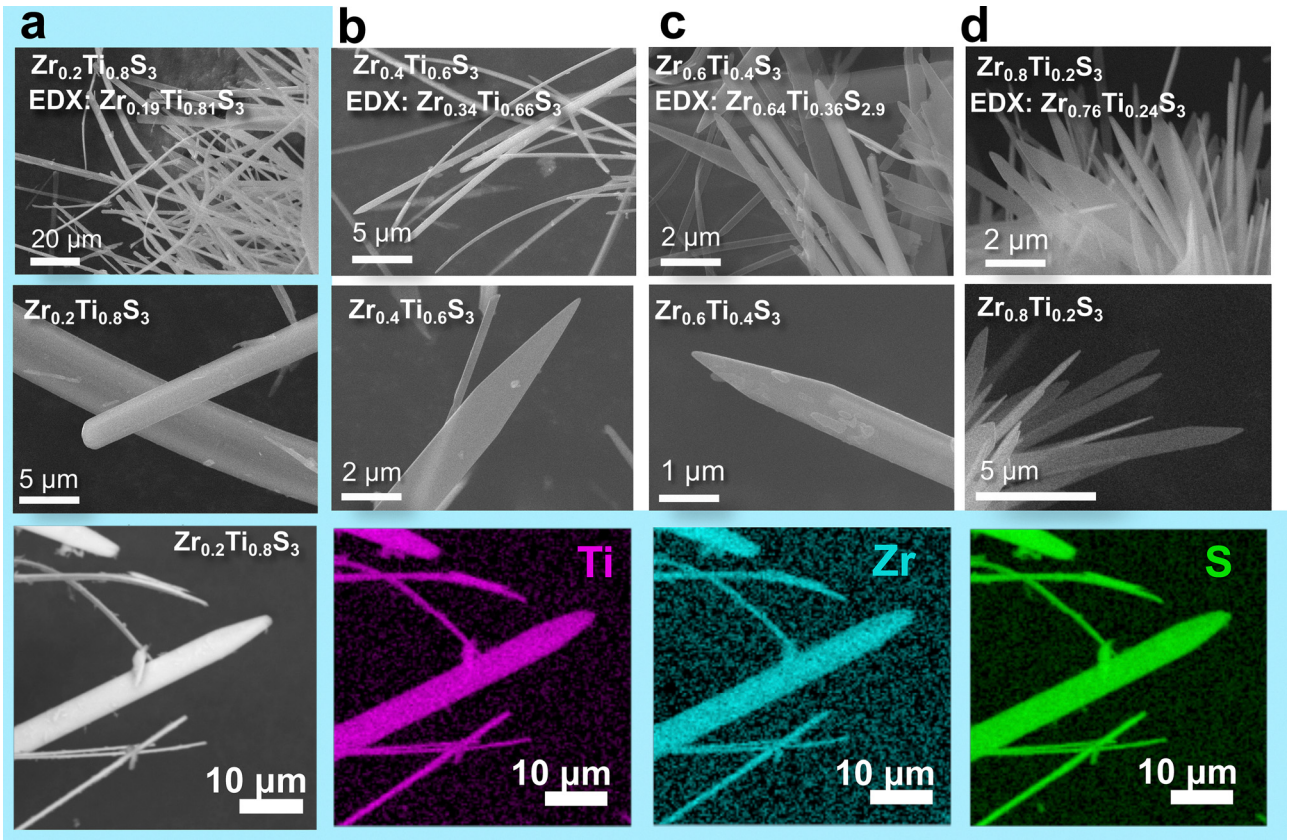

Fig. 2 SEM images (top and middle rows) of $Zr_{1-x}Ti_xS_3$ crystals for the following *x* values: (a) 0.8, (b) 0.6, (c) 0.4, and (d) 0.2. The bottom row belongs to panel (a) and shows SEM image and EDX maps of Ti, Zr and S for $Zr_{0.2}Ti_{0.8}S_3$.

the width of a single ribbon is typically less than 2 μm. It is important to note that all the crystals discussed above and shown in Fig. 2 were synthesized at 600 °C, using comparable masses of alloy precursors, same temperature gradient, and synthesis time. To achieve crystals of the same size for each composition, the synthesis conditions should be individually adjusted for each case.

All $Zr_{1-x}Ti_xS_3$ crystals are reasonably stable in ambient conditions, and their degradation becomes noticeable only after weeks of storage in air. SEM images of samples after long-term storage in air reveals the formation of particles with characteristic shapes of anatase platelets[41] on the surface of $Zr_{1-x}Ti_xS_3$ crystals (Fig. S9), which also correlates with the increased oxygen content in EDX spectra (Fig. S10). In order to ensure that we analyzed pure solid solutions rather than samples containing oxidation products, all the materials characterization was performed on freshly prepared $Zr_{1-x}Ti_xS_3$ crystals.

We studied the effect of chemical composition of solid solutions on their bond vibrations. Fig. 3a shows Raman spectra of all obtained compositions of $Zr_{1-x}Ti_xS_3$ solid solutions, as well as the spectra of pristine ZrS_3 and TiS_3. For the Raman peaks of $Zr_{1-x}Ti_xS_3$ solid solutions we used the same labelling approach as in ref. 42 for ZrS_3 and $ZrSe_3$. We observed a nearly linear change in the position of the A_g^3 peak with the increasing Ti content, from 154 cm^{-1} in pristine ZrS_3 to 179 cm^{-1} in TiS_3, due to the almost twofold difference in atomic masses of Zr and Ti (Fig. 3b). The vibration scheme for this peak is shown in Fig. 3c.

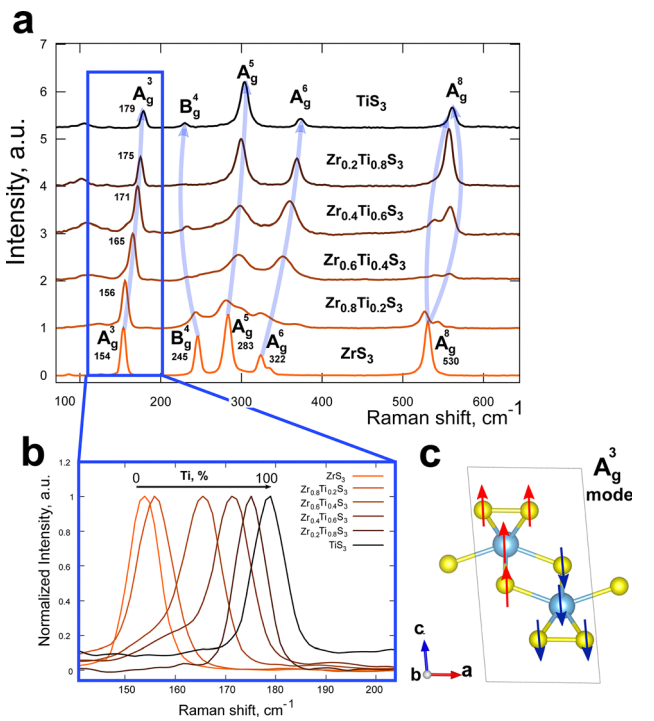

Fig. 3 (a) Raman spectra of $Zr_{1-x}Ti_xS_3$ crystals with (b) the A_g^3 peak position depending on the Ti/Zr ratio in a solid solution and (c) graphical representation of the A_g^3 vibration mode.

We found a different trend for the B_g^4 vibration mode, which is observed at 245 cm^{-1} for ZrS_3. This band was not previously discussed in studies that employed a green 532 nm laser as the excitation source, where the B_g^4 peak was reported to have very low intensity.[42–44] Here, with a 780 nm laser, the B_g^4 mode band is very prominent in ZrS_3 and has a lower intensity in TiS_3. We also note that its intensity inversely correlates with the amount of Ti in the solid solutions, with the lowest intensity observed in $Zr_{0.2}Ti_{0.8}S_3$. The position of the B_g^4 band changes differently compared to the A_g^3 band, being smallest in $Zr_{0.2}Ti_{0.8}S_3$ and largest in ZrS_3 (230 and 245 cm^{-1} respectively).

An interesting observation was made for the highest-frequency band A_g^8 located at 530 cm^{-1} in ZrS_3. This band splits in all studied solid solution crystals, indicating the formation of new vibration modes in the $Zr_{1-x}Ti_xS_3$ system. Finally, the positions of the A_g^5 and A_g^6 bands shift from lower to higher wavenumbers with the increasing Ti content.

The structural parameters of the $Zr_{1-x}Ti_xS_3$ solid solutions were identified using X-ray diffraction (XRD) analysis. The XRD patterns for all synthesized compounds are presented in Fig. 4, while the corresponding lattice parameters are summarized in Table S1. All diffractograms display very similar patterns, with the most intense reflections coming from the (001) and (012) planes (Fig. 4a). The XRD patterns exhibit texture due to the needle-like shape of the crystals. Starting from $2\Theta = 30°$, we observe a gradual shift of the peaks that linearly correlates with the Ti/Zr ratio. The dependence is even more prominent in the waterfall presentation of the XRD data in Fig. 4b. We did not detect any additional superstructure peaks, and the a, b, and c lattice parameters, as well as the unit cell volume show a clear linear dependence on the Zr content (Fig. 4c), in agreement with the Vegard's law.[45] No correlation was found between the angle β and the composition. The gradual shift in lattice parameters is in agreement with the formation of a substitutional solid solution at any given metal ratio.

Finally, we performed diffuse reflectance spectroscopy of $Zr_{1-x}Ti_xS_3$ solid solutions and calculated their optical bandgaps using the conventional Kubelka–Munk function and the Tauc plot approximation for the linear parts of the spectra (Fig. 5a). We note in passing that TMTC compounds are known for rich excitonic physics,[37,46–48] but in this study we specifically focused on the absorption edge energies of $Zr_{1-x}Ti_xS_3$ solid solutions to determine their optical bandgaps. We obtained a close to linear fit of the bandgap values for the investigated $Zr_{1-x}Ti_xS_3$ materials with the composition varying from TiS_3 to ZrS_3, as shown in Fig. 5b. The optical bandgap of $Zr_{1-x}Ti_xS_3$ solid solutions ranges from 1 to 2 eV. All these values fall within the optimal range for many optoelectronic applications.[30] The electronic bandgaps of these compounds should be higher by the values of the corresponding exciton binding energies. While not currently known for $Zr_{1-x}Ti_xS_3$ ($0 < x < 1$), they are likely comparable to TiS_3, for which the exciton binding energy was experimentally shown to be about 0.13 eV.[47]

The ease of exfoliation of TMTC materials through simple ultrasonic treatment in various media allows for the production of ready-to-use inks suitable for slot-die,[29] inkjet,[22] and other printing techniques, opening up numerous potential

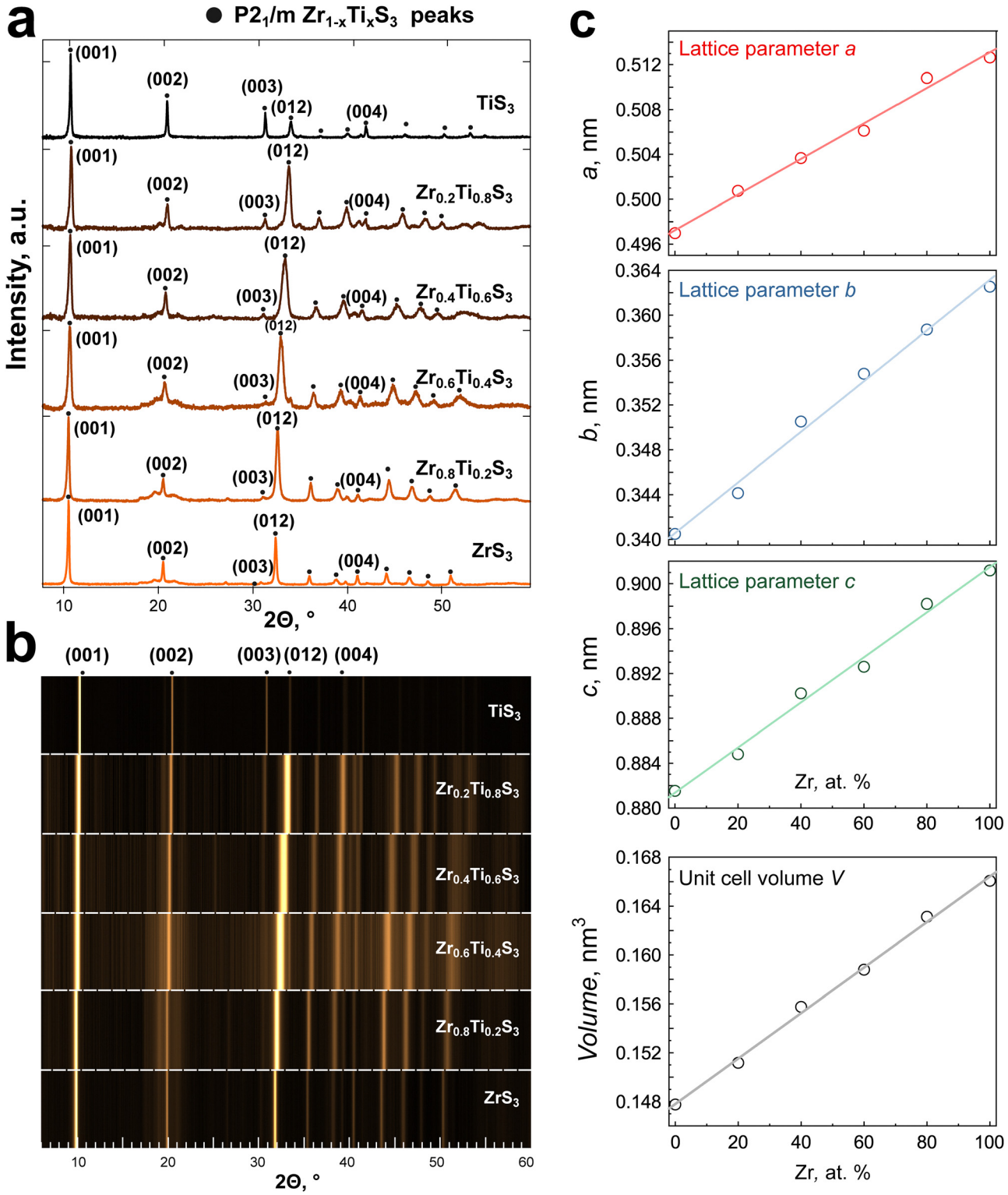

Fig. 4 (a) XRD patterns for all $Zr_{1-x}Ti_xS_3$ solid solution compositions measured with Cu Kα radiation. (b) Waterfall chart showing gradual shift of XRD peaks with the change of composition of solid solutions. (c) Lattice parameters and cell volumes for all $Zr_{1-x}Ti_xS_3$ crystals showing linear dependences on the Zr content as expected for substitutional solid solutions.

applications for $Zr_{1-x}Ti_xS_3$ solid solutions. We also note that while it is also possible to modulate bandgaps of TMTCs by varying the chalcogen ratio in solid solutions like $ZrS_{3-x}Se_x$,[2,49,50] and $ZrTe_{3-x}Se_x$,[51] the use of toxic chalcogens for this purpose, such as Se and Te, is less practical than the more environmentally friendly Ti/Zr substitution.

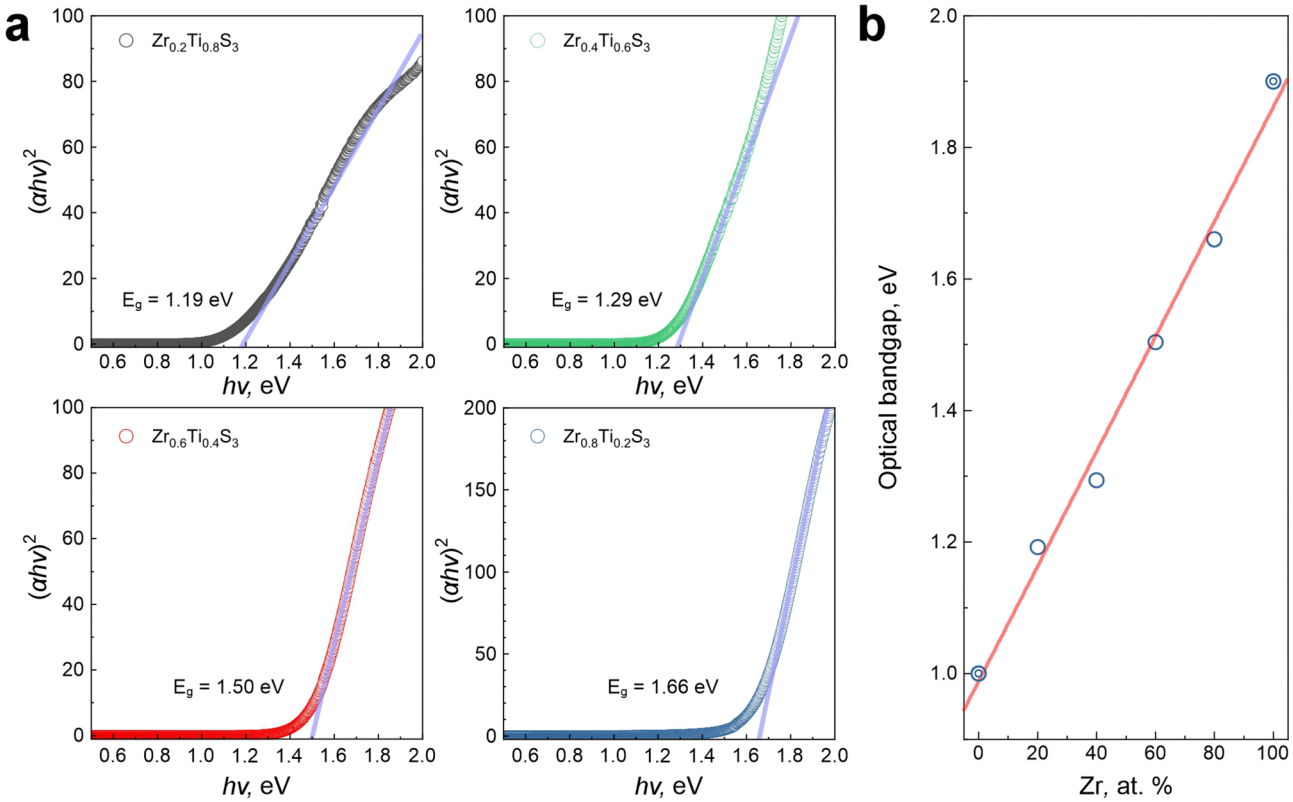

Fig. 5 (a) Kubelka–Munk functions and Tauc plots for the diffuse reflectance spectra measured for $Zr_{1-x}Ti_xS_3$ solid solution powders. (b) Linear fit of $Zr_{1-x}Ti_xS_3$ ($0 \leq x \leq 1$) bandgap values including literature data (bullseye circles) for pristine ZrS_3 (ref. 12) and TiS_3 (ref. 31).

Conclusions

A full range of $Zr_{1-x}Ti_xS_3$ solid solutions with $x = 0.2$ step was successfully synthesized using chemical vapor transport reactions between $Zr_{1-x}Ti_x$ alloys and sulfur vapor in sealed quartz ampoules at 600 °C. The structure and composition of solid solutions were confirmed through XRD, EDX, and Raman measurements. In particular, EDX analysis confirmed uniform distribution of Ti, Zr, and S within the crystals. In line with the Vegard's law, the refined lattice parameters *a*, *b* and *c* of $Zr_{1-x}Ti_xS_3$ crystals display a linear dependence on the Zr content, which is consistent with the formation of substitutional solid solutions.

Our study demonstrates the ability to control the optical bandgap of $Zr_{1-x}Ti_xS_3$ solid solutions by varying the metal ratio in the precursor alloy used for synthesis. The lowest bandgap value of 1.19 eV was determined for $Zr_{0.2}Ti_{0.8}S_3$, while the highest was 1.65 eV for $Zr_{0.8}Ti_{0.2}S_3$. Considering the known bandgaps of TiS_3 and ZrS_3 of about 1 and 2 eV, respectively, the resulting dependence of the bandgap of $Zr_{1-x}Ti_xS_3$ on the Zr content is nearly linear, suggesting a straightforward preparation of solid solutions with desired bandgaps in the 1–2 eV range while maintaining the same $ZrSe_3$-type structure as in pristine TiS_3 and ZrS_3. The study demonstrates a simple and practical route for bandgap engineering in TMTC materials in the technologically important 1–2 eV range, suggesting their relevance to photovoltaics, light-emitting devices and photodetectors for telecommunications, integrated photonics, biomedical imaging, and many other optoelectronic applications.

Experimental

Synthesis of precursor alloys

$Zr_{1-x}Ti_x$ alloys were produced by co-melting of pure Ti and Zr metals using a high-vacuum arc-melting furnace. Titanium and zirconium were mixed in 20/80, 40/60, 60/40, and 80/20 molar ratios, and the chemical compositions of the resulting $Zr_{1-x}Ti_x$ alloys were confirmed by EDX, as shown in Table S2.

Synthesis of $Zr_{1-x}Ti_xS_3$ solid solutions

The $Zr_{1-x}Ti_x$ alloys were ground into coarse particles and sealed under vacuum in separate quartz tubes with elemental sulfur. In a typical synthesis, we used 300–400 mg of a $Zr_{1-x}Ti_x$ alloy and a calculated amount of sulfur for obtaining stoichiometric $Zr_{1-x}Ti_xS_3$ solid solutions. All solid solution crystals were synthesized at 600 °C in a tube furnace (Lenton LHC 12/750). The precursor materials were located directly in the center of the furnace (Fig. 1c), while the other side of the ampoule was kept a few centimeters away from the hot zone, forming a small temperature gradient along the ampoule. For the synthesis of TiS_3 and ZrS_3 crystals, we also prepared similar quartz tubes, in which sulfur was sealed with Ti or Zr powders, respectively. TiS_3 was synthesized at 500 °C while ZrS_3 was obtained at 800 °C.

The produced crystals were then dispersed in isopropyl alcohol (10 mg mL^{-1}) and treated in an ultrasonic bath for 1.5 h to get stable dispersions. These dispersions were then printed with a slot-die Ossila printer on glass slides to test the ink deposition and prepare samples for optical measurements. The resulting samples are shown in the series of optical photographs in Fig. 1d.

Characterization methods

SEM imaging was performed using a Tescan Vega 3 scanning electron microscope with an integrated AZtec EDX module from Oxford Instruments. Raman spectroscopy was performed using a Thermo DXR Raman microscope with a 780 nm solid-state laser. XRD patterns were recorded using a PANalytical X'Pert instrument with Cu Kα radiation. Crystallographic data from the powder X-ray diffraction patterns were obtained using Le Bail profile fitting performed with BGMN package included within Profex software.[52] Diffuse reflectance spectra were measured using a Cary 5000 UV-visible spectrometer.

Author contributions

Dmitry S. Muratov: conceptualization, data curation, formal analysis, investigation, methodology, visualization, writing – original draft, review and editing. Ettore Bianco: investigation. Dmitry Karpenkov: data curation, investigation, methodology. Alberto Castellero: resources, methodology. Alexey Lipatov: data curation, formal analysis, investigation, methodology, visualization, writing – original draft, review and editing. Valter Maurino: formal analysis, funding acquisition, project administration, resources, writing – review & editing. Alexander Sinitskii: conceptualization, data curation, formal analysis, funding acquisition, investigation, project administration, writing – original draft, review and editing.

Conflicts of interest

There are no conflicts to declare.

Data availability

The authors confirm that the data supporting the findings of this study are available within the article or included in SI, any additional data are available on request from the authors.

Refined lattice parameters, EDX spectra and SEM images of crystals and crystal shape description. See DOI: **https://doi.org/10.1039/d5tc02480c**

Acknowledgements

The authors acknowledge support from the Project CH4.0 under the MUR program "Dipartimenti di Eccellenza 2023–2027" (CUP: D13C22003520001). The work was also supported by the National Science Foundation through awards OIA-2044049 (synthesis of solid solutions) and OSI-2329159 (materials characterization). DSM thanks Vladislav Vanyushin for his contribution to the development of the synthetic approach used in this work.[39]

References

1 S. Furuseth, L. Brattås, A. Kjekshus, A. F. Andresen and P. Fischer, *Acta Chem. Scand., Ser. A*, 1975, **29**, 623–631.
2 L. Brattas and A. Kjekshus, *Acta Chem. Scand.*, 1972, **26**, 3441–3449.
3 M. D. Randle, A. Lipatov, I. Mansaray, J. E. Han, A. Sinitskii and J. P. Bird, *Appl. Phys. Lett.*, 2021, **118**, 210502.
4 A. A. Balandin, F. Kargar, T. T. Salguero and R. K. Lake, *Mater. Today*, 2022, **55**, 74–91.
5 M. Chen, L. Li, M. Xu, W. Li, L. Zheng and X. Wang, *Research*, 2023, **6**, 66.
6 S. Ghosh, S. Rumyantsev and A. A. Balandin, *Appl. Phys. Rev.*, 2024, **11**, 21405.
7 A. V. Frolov, A. P. Orlov, F. Gay, A. A. Sinchenko and P. Monceau, *Appl. Phys. Lett.*, 2021, **118**, 213102.
8 M. Randle, A. Lipatov, A. Kumar, C.-P. Kwan, J. Nathawat, B. Barut, S. Yin, K. He, N. Arabchigavkani, R. Dixit, T. Komesu, J. Avila, M. C. Asensio, P. A. Dowben, A. Sinitskii, U. Singisetti and J. P. Bird, *ACS Nano*, 2019, **13**, 803–811.
9 I. G. Gorlova, S. G. Zybtsev and V. Y. Pokrovskii, *JETP Lett.*, 2014, **100**, 256–261.
10 J. Dai and X. C. Zeng, *Angew. Chem., Int. Ed.*, 2015, **54**, 7572–7576.
11 J. O. Island, M. Barawi, R. Biele, A. Almazán, J. M. Clamagirand, J. R. Ares, C. Sánchez, H. S. J. van der Zant, J. V. Álvarez, R. D'Agosta, I. J. Ferrer and A. Castellanos-Gomez, *Adv. Mater.*, 2015, **27**, 2595–2601.
12 H. Yi, S. J. Gilbert, A. Lipatov, A. Sinitskii, J. Avila, J. Abourahma, T. Komesu, M. C. Asensio and P. A. Dowben, *J. Phys. Condens. Matter*, 2020, **32**, 29LT01.
13 M. A. Stolyarov, G. Liu, M. A. Bloodgood, E. Aytan, C. Jiang, R. Samnakay, T. T. Salguero, D. L. Nika, S. L. Rumyantsev, M. S. Shur, K. N. Bozhilov and A. A. Balandin, *Nanoscale*, 2016, **8**, 15774–15782.
14 A. Geremew, M. A. Bloodgood, E. Aytan, B. W. K. Woo, S. R. Corber, G. Liu, K. Bozhilov, T. T. Salguero, S. Rumyantsev, M. P. Rao and A. A. Balandin, *IEEE Electron Device Lett.*, 2018, **39**, 735–738.
15 J. O. Island, A. J. Molina-Mendoza, M. Barawi, R. Biele, E. Flores, J. M. Clamagirand, J. R. Ares, C. Sánchez, H. S. J. van der Zant, R. D'Agosta, I. J. Ferrer and A. Castellanos-Gomez, *2D Mater.*, 2017, **4**, 022003.
16 J. O. Island, M. Buscema, M. Barawi, J. M. Clamagirand, J. R. Ares, C. Sánchez, I. J. Ferrer, G. A. Steele, H. S. J. van der Zant and A. Castellanos-Gomez, *Adv. Opt. Mater.*, 2014, **2**, 641–645.
17 A. Lipatov, P. M. Wilson, M. Shekhirev, J. D. Teeter, R. Netusil and A. Sinitskii, *Nanoscale*, 2015, **7**, 12291–12296.
18 X. Wang, K. Wu, M. Blei, Y. Wang, L. Pan, K. Zhao, C. Shan, M. Lei, Y. Cui, B. Chen, D. Wright, W. Hu, S. Tongay and Z. Wei, *Adv. Electron. Mater.*, 2019, **5**, 1900419.

19 S. Yang, M. Wu, W. Shen, L. Huang, S. Tongay, K. Wu, B. Wei, Y. Qin, Z. Wang, C. Jiang and C. Hu, *ACS Appl. Mater. Interfaces*, 2019, **11**, 3342–3350.
20 S. J. Gilbert, H. Yi, J. S. Chen, A. J. Yost, A. Dhingra, J. Abourahma, A. Lipatov, J. Avila, T. Komesu, A. Sinitskii, M. C. Asensio and P. A. Dowben, *ACS Appl. Mater. Interfaces*, 2020, **12**, 40525–40531.
21 A. Lipatov, J. Abourahma, G. Viswan, K. Acharya, T. R. Paudel, M. J. Loes, S. Bagheri, A. T. N'Diaye, E. Mishra, T. K. Ekanayaka, M. Zaz, J. Rodenburg, A. Dhingra, R. Streubel, P. A. Dowben and A. Sinitskii, *J. Mater. Chem. C*, 2023, **11**, 9425–9437.
22 S. Baraghani, J. Abourahma, Z. Barani, A. Mohammadzadeh, S. Sudhindra, A. Lipatov, A. Sinitskii, F. Kargar and A. A. Balandin, *ACS Appl. Mater. Interfaces*, 2021, **13**, 47033–47042.
23 C. Wang, C. Zheng and G. Gao, *J. Phys. Chem. C*, 2020, **124**, 6536–6543.
24 N. V. Morozova, I. V. Korobeinikov, K. V. Kurochka, A. N. Titov and S. V. Ovsyannikov, *J. Phys. Chem. C*, 2018, **122**, 14362–14372.
25 N. Rafiefard, A. Iraji Zad, A. Esfandiar, P. Sasanpour, S. Fardindoost, Y. Zou, S. J. Haigh and S. H. H. Shokouh, *Microchim. Acta*, 2020, **187**, 117.
26 V. V. Sysoev, A. V. Lashkov, A. Lipatov, I. A. Plugin, M. Bruns, D. Fuchs, A. S. Varezhnikov, M. Adib, M. Sommer and A. Sinitskii, *Sensors*, 2022, **22**, 9815.
27 M. J. Loes, S. Bagheri, N. S. Vorobeva, J. Abourahma and A. Sinitskii, *ACS Appl. Nano Mater.*, 2023, **6**, 9226–9235.
28 C. C. Mayorga-Martinez, Z. Sofer, J. Luxa, Š. Huber, D. Sedmidubský, P. Brázda, L. Palatinus, M. Mikulics, P. Lazar, R. Medlín and M. Pumera, *ACS Nano*, 2018, **12**, 464–473.
29 D. S. Muratov, A. R. Ishteev, D. A. Lypenko, V. O. Vanyushin, P. Gostishev, S. Perova, D. S. Saranin, D. Rossi, M. Auf der Maur, G. Volonakis, F. Giustino, P. O. Å. Persson, D. V. Kuznetsov, A. Sinitskii and A. Di Carlo, *ACS Appl. Mater. Interfaces*, 2019, **11**, 48021–48028.
30 B. R. Sutherland, *Joule*, 2020, **4**, 984–985.
31 H. Yi, T. Komesu, S. Gilbert, G. Hao, A. J. Yost, A. Lipatov, A. Sinitskii, J. Avila, C. Chen, M. C. Asensio and P. A. Dowben, *Appl. Phys. Lett.*, 2018, **112**, 52102.
32 E. Finkman and B. Fisher, *Solid State Commun.*, 1984, **50**, 25–28.
33 I. J. Ferrer, J. R. Ares, J. M. Clamagirand, M. Barawi and C. Sánchez, *Thin Solid Films*, 2013, **535**, 398–401.
34 H. G. Grimmeiss, A. Rabenau, H. Hahn and P. Ness, *Z. Phys. Chem., Abt. A*, 1961, **65**, 776–783.
35 S. Kurita, J. L. Staehli, M. Guzzi and F. Lévy, *Phys. B*, 1981, **105**, 169–173.
36 K. Sieber, B. Fotouhi and O. Gorochov, *Mater. Res. Bull.*, 1983, **18**, 1477–1484.
37 P. Gard, C. Sourisseau and O. Gorochov, *Phys. Status Solidi B*, 1987, **144**, 885–901.
38 P. Gard, F. Cruege, C. Sourisseau and O. Gorochov, *J. Raman Spectrosc.*, 1986, **17**, 283–288.
39 D. S. Muratov, V. O. Vanyushin, N. S. Vorobeva, P. Jukova, A. Lipatov, E. A. Kolesnikov, D. Karpenkov, D. V. Kuznetsov and A. Sinitskii, *J. Alloys Compd.*, 2020, **815**, 152316.
40 W. K. Burton, N. Cabrera and F. C. Frank, *Nature*, 1949, **163**, 398–399.
41 F. Pellegrino, E. Ortel, J. Mielke, R. Schmidt, V. Maurino and V.-D. Hodoroaba, *Adv. Eng. Mater.*, 2022, **24**, 2101347.
42 K. Osada, S. Bae, M. Tanaka, H. Raebiger, K. Shudo and T. Suzuki, *J. Phys. Chem. C*, 2016, **120**, 4653–4659.
43 A. Zwick, M. A. Renucci and A. Kjekshus, *J. Phys. C-Solid State Phys.*, 1980, **13**, 5603–5614.
44 J. Y. Harbec, C. Deville Cavellin and S. Jandl, *Phys. Status Solidi*, 1979, **96**, K117–K120.
45 L. Vegard, *Z. Phys*, 1921, **5**, 17–26.
46 K. N. Boldyrev, E. V. Mostovshchikova, A. N. Titov, V. Y. Pokrovskii and I. G. Gorlova, *JETP Lett.*, 2024, **120**, 565–572.
47 A. J. Molina-Mendoza, M. Barawi, R. Biele, E. Flores, J. R. Ares, C. Sánchez, G. Rubio-Bollinger, N. Agraït, R. D'Agosta, I. J. Ferrer and A. Castellanos-Gomez, *Adv. Electron. Mater.*, 2015, **1**, 1500126.
48 Q. Cui, A. Lipatov, J. S. Wilt, M. Z. Bellus, X. C. Zeng, J. Wu, A. Sinitskii and H. Zhao, *ACS Appl. Mater. Interfaces*, 2016, **8**, 18334–18338.
49 A. Zwick, G. Landa, R. Carles, M. A. Renucci and A. Kjekshus, *Solid State Commun.*, 1983, **45**, 889–893.
50 J. Deslandes and S. Jandl, *Phys. Rev. B: Condens. Matter. Mater. Phys.*, 1984, **29**, 2088–2090.
51 X. Zhu, W. Ning, L. Li, L. Ling, R. Zhang, J. Zhang, K. Wang, Y. Liu, L. Pi, Y. Ma, H. Du, M. Tian, Y. Sun, C. Petrovic and Y. Zhang, *Sci. Rep.*, 2016, **6**, 26974.
52 N. Doebelin and R. Kleeberg, *J. Appl. Crystallogr.*, 2015, **48**, 1573–1580.

